
Modelling mushy zones in welds of multicomponent alloys: implications for solidification cracking

J. N. DuPont, C. V. Robino, and A. R. Marder

A method is proposed for calculating the variation in fraction liquid with distance in the mushy zone as an aid to determining the effect of alloy additions on solidification cracking susceptibility. The model combines the general liquidus equation of a multicomponent system, solute redistribution relations, and temperature gradient information. Calculations are presented for a range of niobium bearing superalloys and the results were found to reveal important relations between alloy composition, variation in fraction liquid with distance in the mushy zone, and cracking susceptibility as measured by the Varestraint test. In particular, the results directly show that the addition of carbon to these alloys is generally beneficial because it reduces the size of the crack susceptible mushy zone and limits the amount of terminal liquid available for the low temperature $L \rightarrow \gamma + \text{Laves}$ reaction. The modelling results and experimental data are also used to describe the influence of other alloy additions.

Dr DuPont and Dr Marder are at the Whitaker Laboratory, Lehigh University, 5 East Packer Avenue, Bethlehem, PA18015, USA, and Dr Robino is in the Materials Joining Department, Sandia National Laboratories, Albuquerque, NM87185, USA. Manuscript received 24 October 1997; in final form 10 August 1998.

© 1999 IoM Communications Ltd.

INTRODUCTION

The solidification cracking susceptibility of engineering alloys is known to be highly dependent on the solidification temperature range and the amount and distribution of liquid which exists at the terminal stages of solidification.^{1,2} Nominal alloy composition and redistribution of solute (microsegregation) play important roles in solidification cracking as ultimately they control the solidification temperature range and amount of eutectic liquid. Under conditions of high cooling rate, such as may exist in laser and electron beam processes, significant dendrite tip undercooling can occur, which minimises the extent of microsegregation and, as a result, will also contribute to the final solidification temperature range and amount of eutectic constituent. Such undercooling effects are not considered in the present work. Previous studies conducted to quantify fundamentally the relation between alloy composition, microsegregation, and cracking tendency often used binary alloy systems.^{1,2} This approach is useful as it readily permits microsegregation calculations to be performed because the appropriate alloy parameters (e.g. liquidus temperature, distribution coefficient, eutectic temperature, and composition) can be determined directly from the simple binary phase diagram.

Many alloys of engineering significance contain multiple solute additions and can undergo one or more eutectic type reactions over a broad temperature and composition range. In this case, microsegregation calculations require knowledge of multicomponent phase diagrams and the distribution coefficients for all solutes which significantly affect development of the final microstructure. In addition, when a eutectic type reaction occurs over an appreciable temperature and composition range, it then becomes necessary to know two distribution coefficients for each important solute; one which describes solute partitioning between the liquid and primary solid phase and a second which describes partitioning between the liquid and secondary solid phase within the eutectic constituent. The lack of such information tends to limit the application of solute redistribution modelling to understanding the weldability of multicomponent alloys of engineering significance. However, in recent years there has been considerable progress in the development of thermodynamic software programs for calculating solidification parameters and phase diagrams of multicomponent systems.³ This progress is likely to lead to more frequent use of solute redistribution models which can be applied to alloy systems containing many elements. In view of this fact it is useful to consider how such modelling efforts can be applied to the understanding of weldability phenomena.

In previous work the present authors reported results of a study aimed at measuring solidification parameters and modelling solute redistribution of experimental alloys that simulate the solidification behaviour observed in many commercial niobium bearing superalloys.^{4,5} These alloys are used extensively in many applications requiring high temperature strength and good resistance to oxidation. The model permits the relationship between temperature, liquid composition, and fraction liquid to be determined during the solidification process. In the present work modelling information is applied to calculate the variation in fraction liquid within the crack susceptible mushy zone of these multicomponent alloys as an aid to understanding Varestraint solidification cracking results. It should be noted that the analysis described is general in nature and can be applied to any alloy system when the appropriate solidification parameters are relatively constant and interactive effects are not large. Interactive effects, which may occur when the partitioning behaviour of a solute element between the liquid and the solid is a function of the concentration level of another alloying element, can be handled with extended analyses. However, such an approach is avoided in the present work in order to keep the concepts tractable by minimising mathematical manipulations.

EXPERIMENTAL

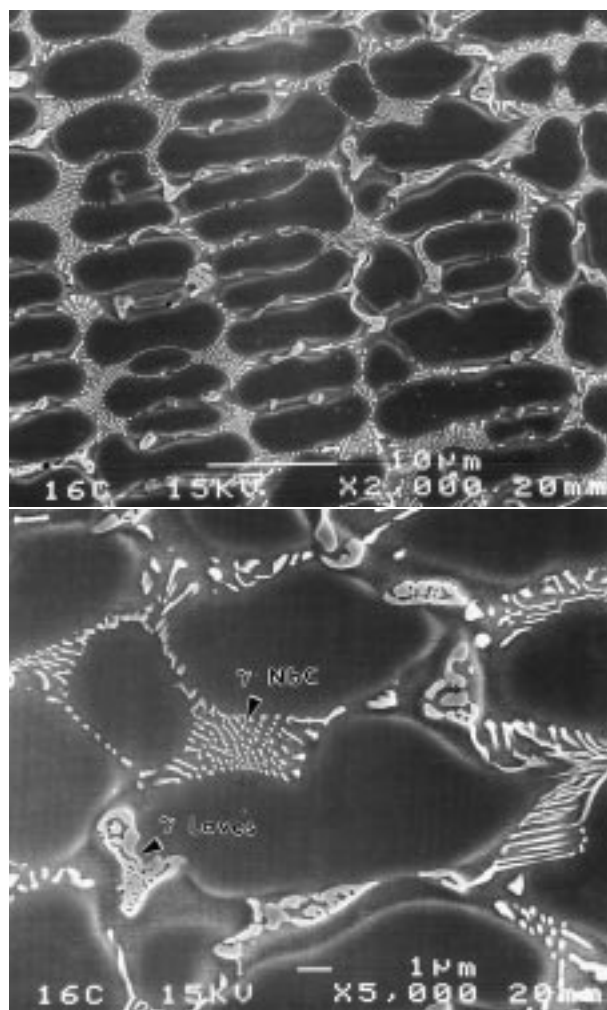
The experimental procedures used in the present work are described in detail elsewhere and are not repeated here.⁴ Alloy compositions used to simulate commercial alloys of interest are given in Table 1. The alloys contained factorial variations in iron (in exchange for nickel), niobium, silicon,

and carbon at two levels. The high and low target levels of niobium, silicon, and carbon were set as $2 < \text{Nb} < 5$, $0.10 < \text{Si} < 0.60$, and $0.02 < \text{C} < 0.15$ (wt-%). These limits were chosen to represent low and high composition values of wrought alloys and filler metals as well as composition limits that can arise in fusion welds made between nickel base alloys and carbon steels. Several additional alloys with intermediate carbon contents (alloys 1.5, 3.5, 7.5, and 12) were also investigated.

Differential thermal analysis (DTA) was conducted on a Netzsch STA 409 differential thermal analyser using 500–550 mg specimens. Liquidus and solidus temperatures were determined from slow heating rate (5 K min^{-1}) scans and temperatures of eutectic type reactions that occurred during solidification were measured with faster cooling rate (20 K min^{-1}) scans. Solidification cracking susceptibility was evaluated using the Varestraint test at an augmented strain of 2.5% to simulate highly restrained welds.^{6,7} The specimens were machined to subsize Varestraint specimen dimensions ($165 \times 25 \times 3.2 \text{ mm}$). Welds were produced using current 95 A, voltage 10 V (2.5 mm arc gap), and travel speed 3.3 mm s^{-1} with high purity argon at a flowrate of 17 L min^{-1} . A 3.2 mm diameter W-2ThO₂ electrode was used with a 60° tip angle. These conditions produced welds 4.5 mm wide and 6.5 mm long. In order to acquire adequate statistics, three tests were conducted on each alloy at an augmented strain of 2.5% to simulate highly restrained welds. The maximum crack length (MCL) was used as the indicator of cracking susceptibility and was measured using a light optical microscope at a magnification of 100. Microstructural characterisation of weld metal and Varestraint specimens was conducted by light optical microscopy, scanning electron microscopy (SEM), quantitative image analysis (QIA), and electron probe microanalysis (EPMA).

BACKGROUND

A brief review of previous results and interpretations is given below as a framework for discussion in the subsequent section which links the model calculations to weldability data.^{4,5} A typical weld metal microstructure is shown in Fig. 1. In addition to the primary γ dendrites, the microstructures generally contain two eutectic type constituents, γ -NbC and γ -Laves. The individual amounts of the γ -NbC and γ -Laves constituents were large enough in a number of



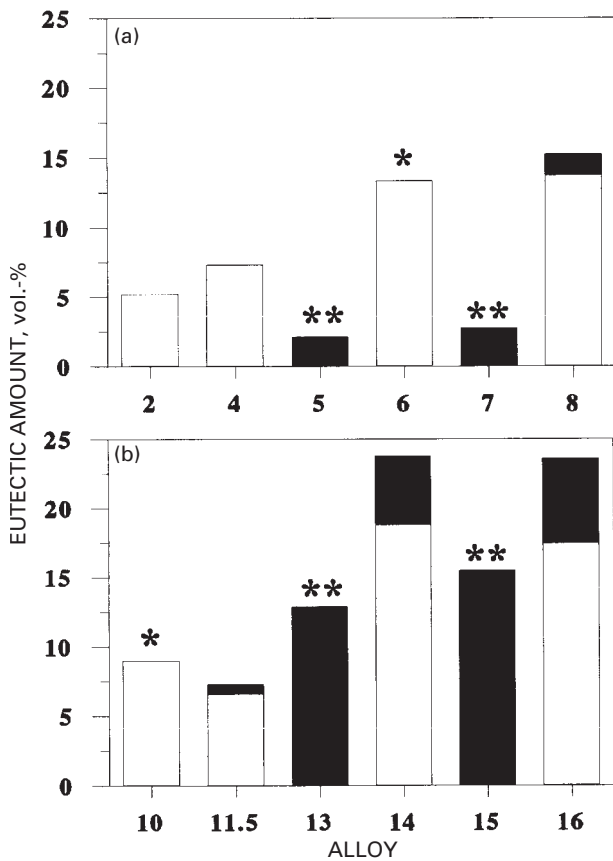
1 Scanning electron micrographs showing weld metal microstructure of alloy 16

alloys to quantify by QIA and these results are shown in Fig. 2. Specimens for QIA were electrolytically etched in a solution of 10% chromic acid + 90% water at 3 V and area fractions were measured along the centreline of each weld (at locations far removed from the solidification cracks) with at least ten SEM images. Area fractions were assumed to be equivalent to volume fractions. The results from nickel base and iron base alloys are aligned to permit comparisons between alloys with similar solute levels. Carbon additions promote formation of the γ -NbC constituent while iron and silicon increase the amount of the γ -Laves constituent.^{4,5} The effect of niobium depends on the carbon content. At high carbon levels, niobium additions will promote formation of γ -NbC. When the carbon level is low, niobium generally promotes formation of the γ -Laves constituent. These effects have been documented in commercial alloy systems also.^{8,9}

The solidification reactions in these experimental multicomponent alloys are similar to those expected in ternary Ni-Nb-C alloys and this system was used as a basis for developing a pseudoternary solidification model.^{10,11} The multicomponent alloys were modelled as a ternary system by grouping together the iron, nickel, and chromium matrix elements to form the γ 'component' of the γ -Nb-C system. Solute redistribution of niobium and carbon between the liquid and solid phases was modelled using the approach developed by Mehrabian and Flemings,¹² with modifications made to account for the high diffusion rate of carbon in the solid.^{5,13} Values for the equilibrium distribution coefficient k (where $k = C_s/C_l$, C_s is the solid composition, and C_l is the liquid composition) of niobium and

Table 1 Compositions of alloys used, wt-%

Alloy	Fe	Ni	Cr	Nb	Si	C	P	S
Ni base alloys								
1	10.49	68.53	18.90	1.93	0.08	0.017	0.004	0.003
1.5	10.75	67.95	19.21	2.00	0.03	0.052	0.004	0.003
2	11.12	68.20	19.12	1.95	0.06	0.132	0.004	0.002
3	10.70	68.11	19.02	1.82	0.38	0.010	0.004	0.003
3.5	10.39	66.80	19.29	1.94	0.41	0.075	0.004	0.003
4	10.72	67.60	19.08	1.91	0.40	0.155	0.004	0.001
5	10.84	65.79	18.98	5.17	0.05	0.013	0.005	0.010
6	10.88	65.22	18.89	4.87	0.08	0.161	0.005	0.007
7	10.70	65.53	19.30	4.86	0.52	0.010	0.005	0.009
7.5	10.82	63.93	18.54	4.92	0.46	0.081	0.005	0.004
8	10.80	64.96	18.90	4.72	0.52	0.170	0.005	0.007
Fe base alloys								
9	46.03	33.56	19.31	1.66	0.10	0.003	0.006	0.003
10	46.69	32.80	19.70	1.66	0.01	0.108	0.006	0.002
11	45.38	32.80	19.53	1.77	0.57	0.004	0.006	0.002
11.5	47.38	31.05	19.64	1.84	0.67	0.116	0.006	0.001
12	45.28	32.39	19.89	1.93	0.61	0.079	0.006	0.002
13	44.55	31.24	19.63	4.42	0.02	0.015	0.007	0.003
14	44.05	31.93	19.52	4.51	0.08	0.210	0.006	0.002
15	45.40	30.03	19.54	4.88	0.66	0.010	0.007	0.003
16	44.47	30.89	19.45	4.77	0.64	0.216	0.006	0.002



* contained very small amount of Laves phase which could not be quantified; ** contained very small amounts of NbC phase which could not be quantified
 ■ γ -Laves; □ γ -NbC
 a for Ni base alloys; b for Fe base alloys

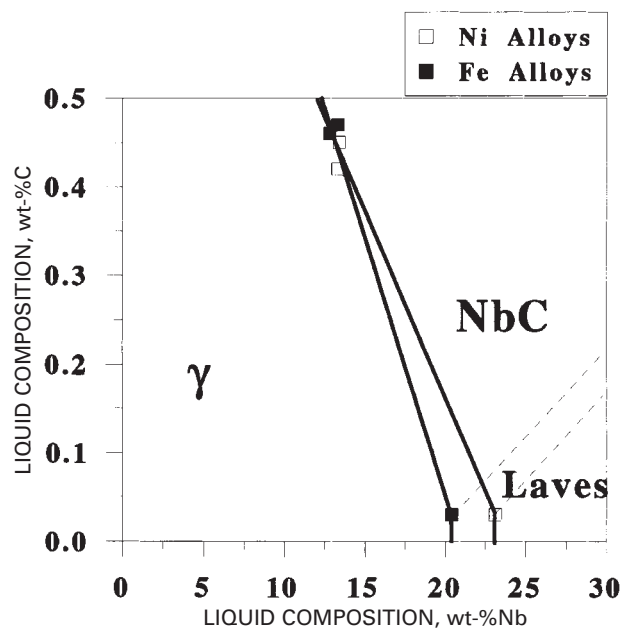
2 Results from QIA showing individual amounts of γ -Laves and γ -NbC constituents

carbon were measured using EPMA and DTA respectively. The EPMA measurements were performed using a Jeol 733 probe equipped with four wavelength dispersive spectrometers. Measurements were made on welds prepared with no forced cooling as well as welds in which the dendrite tips were quenched with a water jet spray as they grew into the advancing weld pool.⁴ These values are summarised in Table 2 along with *k* values for silicon and the 'solvent' elements (iron, nickel, and chromium). Note that the *k* values for the solvent elements are all similar and close to unity. This indicates they all behave in a similar manner and exhibit little tendency for segregation during solidification, thus justifying the approach of grouping together these elements as the γ 'component' in the γ -Nb-C pseudoternary approach. The equilibrium distribution coefficient for niobium is lower in the iron base alloys (0.25) than in the nickel base alloys (0.46). This indicates that niobium segregates more aggressively to the liquid in the iron base alloys. For this reason, two separate liquidus surface projections were determined to account for this behaviour (Fig. 3), one for the iron base alloys and one for the nickel

Table 2 Distribution coefficients

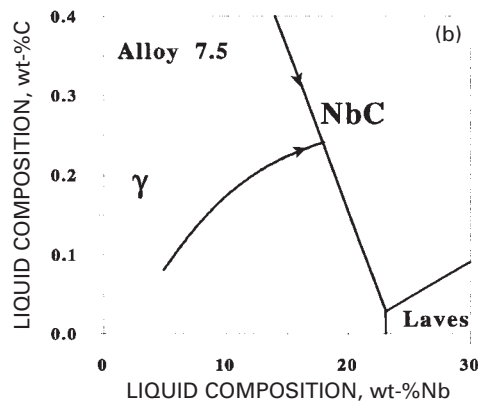
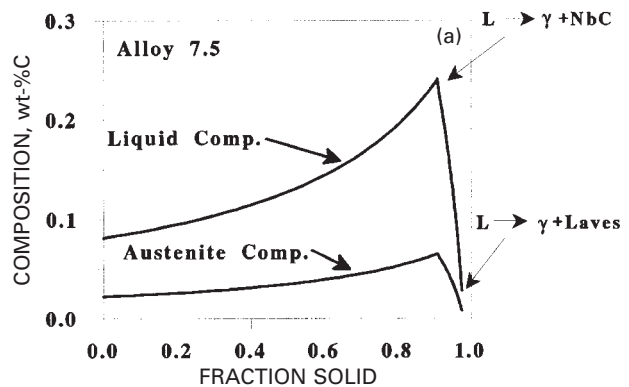
Alloy	Fe	Ni	Cr	Nb	C	Si
Ni base	1.00	1.02	1.06	0.46	0.27	0.71
Fe base	1.06	1.00	1.02	0.25	0.27*	0.58

* Estimated from Ni base alloy data.



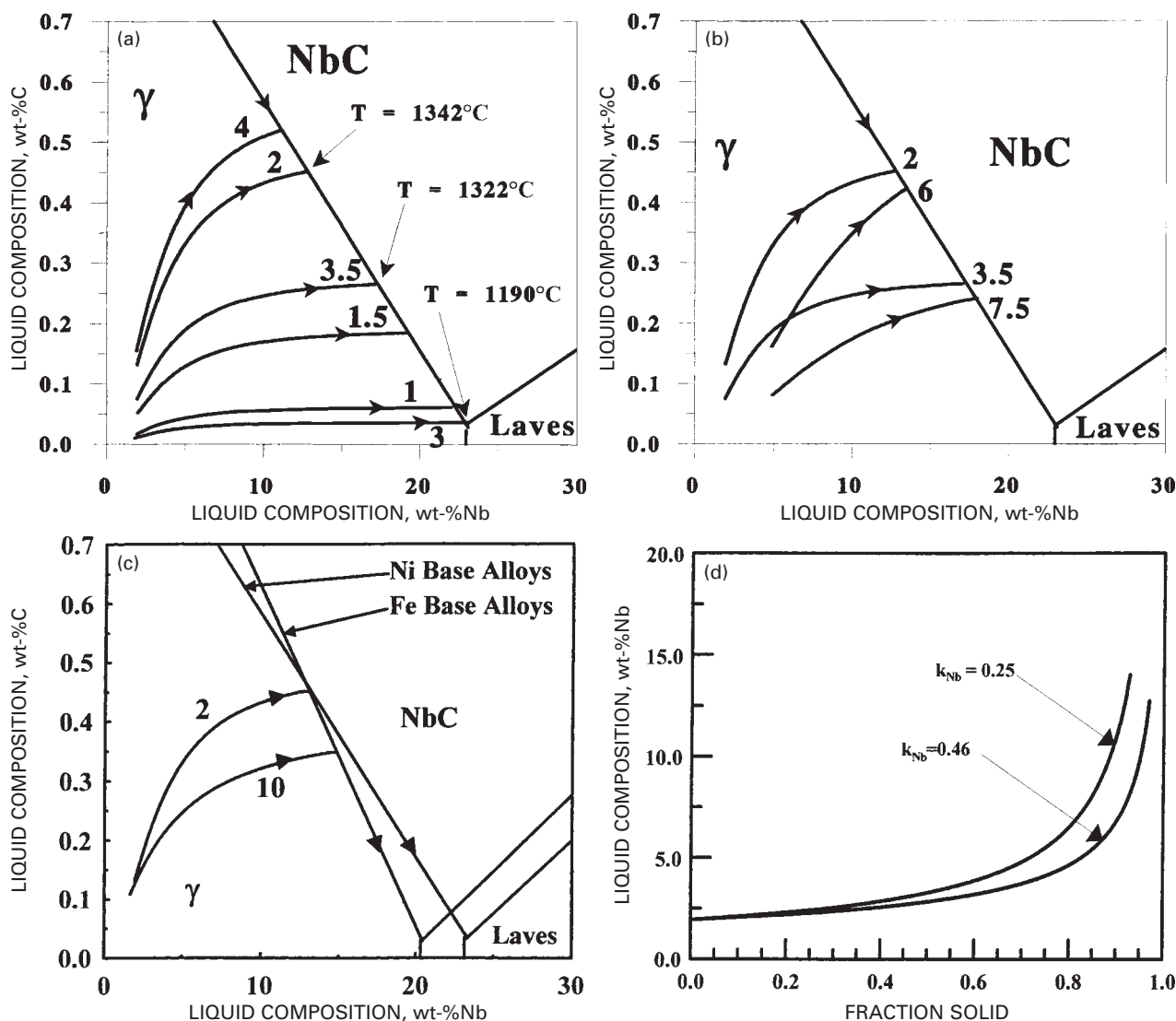
3 Experimentally determined pseudoternary solidification surfaces for Ni base and Fe base alloys

base alloys. The assumptions in the solute redistribution model include negligible dendrite tip undercooling; thermodynamic equilibrium at the solid/liquid interface; infinitely fast diffusion in the liquid; and constant values of equilibrium distribution coefficients. For niobium the assumption of negligible diffusion in the solid is invoked whereas carbon is assumed to diffuse infinitely fast in the solid. The latter assumption for carbon should be reasonably valid because of the high diffusivity of carbon in



a variation in C content in γ and liquid phases during solidification; b calculated primary solidification path superimposed on pseudobinary solidification surface

4 Solute redistribution calculation results for alloy 7.5



a for Ni base alloys with similar Nb contents and variations in C; b for Ni base alloys with similar C contents and variations in Nb; c for Ni base and Fe base alloys with similar contents of solute elements Nb, Si, and C; d variation in liquid composition with fraction solid for two alloys of equivalent nominal Nb content of 1.95 wt-% and different k_{Nb} values

5 Calculated primary solidification path relations superimposed on pseudoternary solidification surface

austenite as discussed in general by Clyne and Kurz¹³ and in particular for the alloys of interest to the present study.^{4,5}

Figure 4 shows typical calculation results (using alloy 7.5 as an example) for the entire solidification process. Figure 4a shows the variation in carbon content in the γ and liquid phases during solidification. Primary $L \rightarrow \gamma$ solidification occurred until there was 0.10 volume fraction liquid remaining with 0.24 wt-%C, at which point the $L \rightarrow \gamma + \text{NbC}$ reaction initiated. The $L \rightarrow \gamma + \text{NbC}$ reaction depleted the liquid of carbon until there was 0.02 volume fraction remaining liquid at 0.03 wt-%C, at which point the $L \rightarrow \gamma + \text{Laves}$ reaction is initiated. Calculations were terminated at this point and the alloy is predicted to have a 0.10 volume fraction of total eutectic type constituent (0.08 volume fraction $\gamma\text{-NbC}$ and 0.02 volume fraction $\gamma\text{-Laves}$). The various phases of interest have similar densities, so there is no need to convert between units of vol-% and wt-%.¹⁴ Niobium and carbon content in the liquid during solidification is superimposed on the pseudoternary surface in Fig. 4b to show this general progression of solidification. The measured and calculated values of the individual eutectic type constituents for all the alloys were compared to validate the approach and the calculated values were generally within the experimental errors of the measured values.¹⁵

Results of typical primary solidification path calculations are shown in Fig. 5 for a number of alloys to reveal the effect of alloy composition. Figure 5a plots typical results for the nickel base alloys that have similar niobium levels but variations in carbon content. Figure 5b compares the solidification paths of nickel base alloys with similar carbon contents and variations in niobium, and Fig. 5c compares the solidification paths of a nickel base and an iron base alloy with similar levels of solute elements (niobium, silicon, and carbon). The alloy number of each path is noted in Fig. 5. Assuming that any change in liquidus slope is not large over the region of interest, the amount of solid formed during primary solidification is approximately proportional to the length of the primary solidification path. This is useful for making quick, qualitative interpretations of the results. The start temperature of the $L \rightarrow \gamma + \text{NbC}$ reaction, as determined by DTA, was noted at several locations along the line of twofold saturation. The point of intersection between the primary solidification path and line of twofold saturation is a strong function of carbon content. As the nominal carbon content increased, the intersection point occurred at higher carbon contents. As a result, the liquid composition must 'travel' a long distance down the $L \rightarrow \gamma + \text{NbC}$ line of twofold saturation, forming $\gamma\text{-NbC}$ as

it travels, before the γ -Laves constituent can form. At a given carbon content, the niobium concentration also had a significant effect on the primary solidification path. This is revealed by comparing alloy 2 with alloy 6 and alloy 3.5 with alloy 7.5 in Fig. 5b. When niobium content was low, the carbon content in the liquid increased relatively quickly during the early stages of solidification. The rate of carbon enrichment continually decreased as the line of twofold saturation was approached. Since the lengths of the primary solidification paths for the high niobium alloys are shorter these alloys will exhibit more liquid at the intersection point, i.e. more total eutectic type constituent. The effect of matrix composition is shown in Fig. 5c. Alloys 2 and 10 have very similar total solute contents but different matrix compositions. Thus, the difference in this case lies in the value of k_{Nb} (k_{Nb} is 0.46 in the nickel base alloys and 0.25 in the iron base alloys). As k_{Nb} was reduced, niobium segregated more aggressively to the liquid. This is demonstrated in Fig. 5d, where the niobium content in the liquid is plotted as a function of fraction solid for two hypothetical alloys with identical nominal niobium concentrations of 1.95 wt-% but different k_{Nb} values. The curves are terminated at the point where the $L \rightarrow \gamma + NbC$ reaction began. Calculations were made at identical nominal niobium concentrations so that the effect of the equilibrium distribution coefficient could clearly be discerned. At any particular value of fraction solid during solidification, an iron base alloy with a k_{Nb} value of 0.25 will always possess more niobium in the liquid than a nickel base alloy with k_{Nb} of 0.46. As a result, the iron base alloys will have more liquid remaining after primary solidification, i.e. less solid. This effect from the reduced k_{Nb} value is the reason for the larger amount of total eutectic type constituents observed in the iron base alloys.

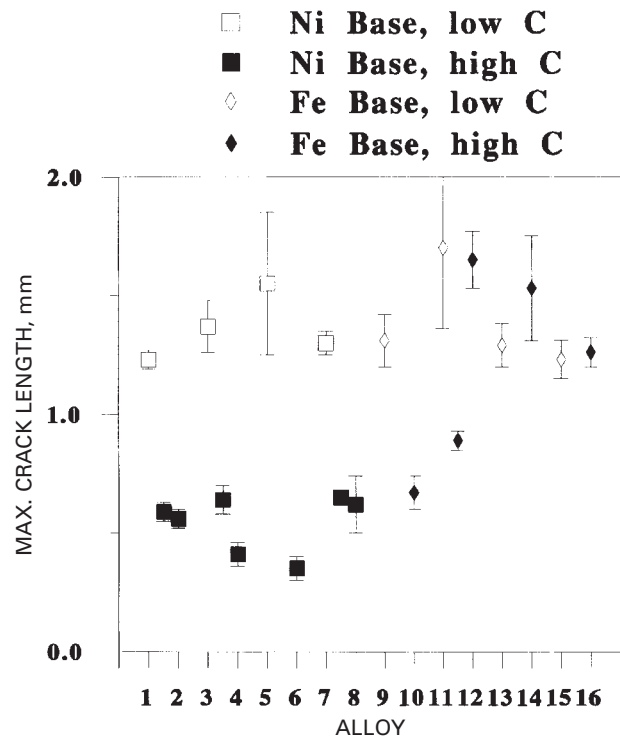
RESULTS AND DISCUSSION

Weldability

Figure 6 shows the MCL for each alloy. The data reported are averages and standard deviations from at least three tests. For the nickel base alloys, there is clear separation in the behaviour among the low carbon alloys (≤ 0.017 wt-%C) with relatively poor weldability from that among the high carbon alloys (≥ 0.052 wt-%C) which showed very good resistance to solidification cracking. Within the iron base alloys, the addition of carbon was only beneficial when the niobium content is low (≤ 1.8 wt-%), and the carbon level must be above ~ 0.10 wt-% to provide the advantageous effect. For example, alloys 11.5 and 12 have essentially identical levels of all other elements except carbon (alloy 12 contains 0.079 wt-%C and alloy 11.5 contains 0.116 wt-%C). This small variation in carbon content led to a substantial difference in the MCL values. Within the iron base alloys with high niobium (alloys 13–16), carbon had no beneficial effect even at the 0.21 wt-% level. A qualitative interpretation of these results, based on the solidification temperature range and fusion zone microstructures, has been described elsewhere.¹⁶ A more quantitative approach is proposed below.

Mushy zone modelling

Conventional solidification cracking concepts qualitatively relate cracking propensity to the amount and distribution of liquid in the mushy zone and the size of the mushy zone.¹⁷ Solute redistribution models can be useful for a priori assessment of these relationships when they are combined with knowledge of the general liquidus equation. The objective of combining such information is to develop plots that, for a fixed set of processing parameters (i.e. with a fixed temperature gradient), reveal how the size of the



6 Maximum crack length for each alloy

mushy zone and variation in fraction liquid within the mushy zone can change with alloy additions.

Ignoring possible interactive effects among the solutes and assuming that the liquidus slopes are constant, the liquidus equation for any multicomponent system is given by⁴

$$T_l = T_0 + \sum m_{i,i} C_{i,i} \dots \dots \dots (1)$$

where $m_{i,i}$ is the liquidus slope for the i th solute in the system, $C_{i,i}$ is the concentration of the i th solute in the liquid, T_l is the liquidus temperature, and T_0 is the melting temperature of the pure solvent. In the present alloys of interest the solutes are assumed to be niobium, silicon, and carbon while the Fe-Ni-Cr ' γ matrix' is treated as the solvent.

It has been shown that the diffusion of niobium and silicon in the solid during solidification is insignificant and solute redistribution of these elements can therefore be described using the Scheil equation.^{4,14,18} Thus, the relationship between $C_{i,i}$ and the fraction liquid f_l for these two elements during primary $L \rightarrow \gamma$ solidification is given by

$$C_{i,Nb} = C_{0,Nb} f_l^{k_{Nb}-1} \dots \dots \dots (2a)$$

$$C_{i,Si} = C_{0,Si} f_l^{k_{Si}-1} \dots \dots \dots (2b)$$

where C_0 is the nominal solute concentration. For carbon the diffusion rate is high enough to permit use of the lever law and the relation between $C_{i,i}$ and f_l is given by^{4,13}

$$C_{i,C} = C_{0,C} / [f_l + k_C(1 - f_l)] \dots \dots \dots (2c)$$

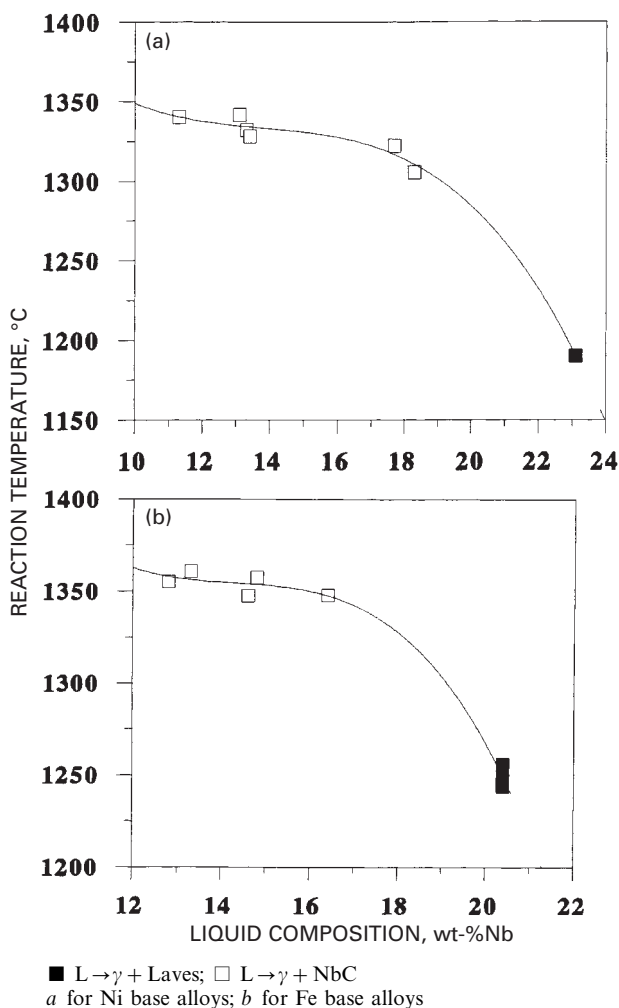
Inserting equations (2) into equation (1) yields the relationship between temperature and f_l

$$T_l = T_0 + m_{i,Nb} C_{0,Nb} f_l^{k_{Nb}-1} + m_{i,Si} C_{0,Si} f_l^{k_{Si}-1} + m_{i,C} C_{0,C} / [f_l + k_C(1 - f_l)] \dots \dots \dots (3)$$

Thus, when the liquidus slopes and distribution coefficients are known, the variation in f_l with temperature during primary solidification can be calculated.

The variation in f_l with distance in the mushy zone can be determined by combining equation (3) with the temperature gradient. The temperature gradient is given by the

Published by Maney Publishing (c) IOM Communications Ltd

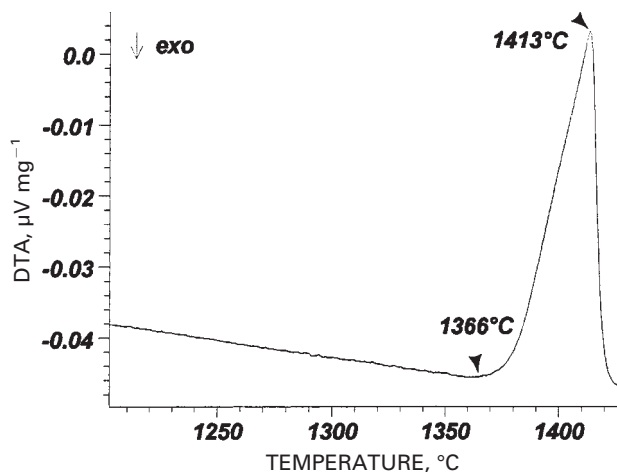


7 Temperatures of $L \rightarrow \gamma + NbC$ and $L \rightarrow \gamma + Laves$ reactions as function of Nb content in liquid

ratio of cooling rate/growth rate. Under these conditions, where a slow travel speed (3.3 mm s^{-1}) was used and the welds were circular, the growth rate at the weld centreline (where typically the MCL develops) was generally equivalent to or approximated by the travel speed. The travel speed in the present case was 3.3 mm s^{-1} and the cooling rate for this set of processing parameters (arc current 95 A, arc voltage 10 V, travel speed 3.3 mm s^{-1}) was estimated to be 660 K s^{-1} through dendrite arm spacing measurements.⁴ Thus, the temperature gradient G was $\sim 200 \text{ K mm}^{-1}$. The variation in G with processing parameters, and its effect on the mushy zone characteristics can also be assessed. However, this relation is fairly straightforward and only the more important influence of alloy composition is considered in the present discussion. At the trailing edge of the weld pool, the liquid is at the liquidus temperature of the alloy $T_{l,0}$. Assuming that G is constant and taking $x = 0$ at $T_{l,0}$, the relation between temperature and distance in the mushy zone is given by

$$x = (T_{l,0} - T)/G \dots \dots \dots (4)$$

where x is the distance behind the weld pool along the weld centreline and G is the temperature gradient along the weld centreline. When $x = 0, f_1 = 1$. Thus, equations (3) and (4) can be combined to determine the variation in f_1 with distance in the mushy zone during the primary solidification stage. When the $L \rightarrow \gamma + NbC$ reaction begins, the relation between f_1 and C_1 is that previously modelled in Ref. 5. At this point, the relatively minor effect of silicon is ignored and only the relation between $f_1, C_{1,Nb}$, and $C_{1,C}$ is considered. Once the relation between f_1 and $C_{1,Nb}$ is established



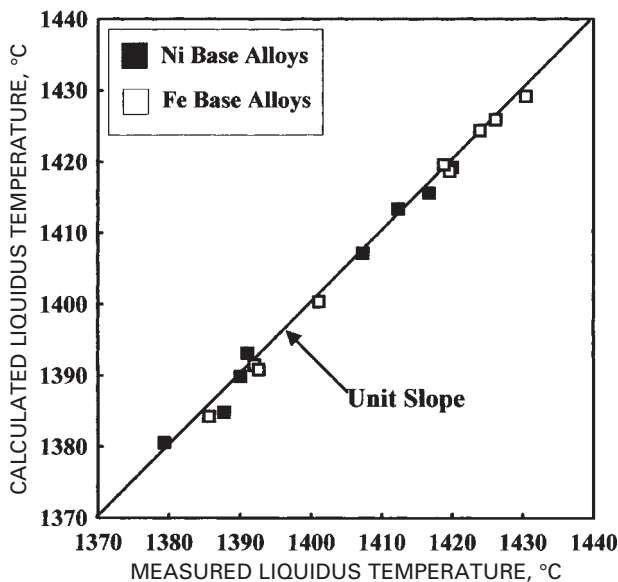
8 Differential thermal analysis heating curve for alloy 3

during the $L \rightarrow \gamma + NbC$ reaction, a relation between temperature and liquid composition during the eutectic type transformations is needed. Such a relation is provided in empirical form in Fig. 7, where the temperature of the lines of twofold saturation (measured by DTA) are plotted as a function of $C_{1,Nb}$. The values of $C_{1,Nb}$ (i.e. the composition of the liquid at the start of the $L \rightarrow \gamma + NbC$ or $L \rightarrow \gamma + Laves$ reactions) were both determined experimentally and calculated using the solute redistribution model.¹⁹ Experimental values were determined by measuring the average composition of the eutectic type constituents using EPMA techniques described elsewhere.⁴ The lines in the plots are the best fits obtained using a third order polynomial. Therefore, the relation between f_1 and $C_{1,Nb}$ can be connected to the empirical relation between temperature and $C_{1,Nb}$ in Fig. 7 to establish the relation between f_1 and temperature during the $L \rightarrow \gamma + NbC$ reaction, which is then combined with equation (4) to describe the relation between f_1 and x in the mushy zone during the $L \rightarrow \gamma + NbC$ reaction. The $L \rightarrow \gamma + Laves$ reaction occurs over a relatively narrow temperature range and is therefore estimated to occur isothermally.^{4,14} Thus, the point at which the liquid composition satisfies conditions for the $L \rightarrow \gamma + Laves$ reaction is taken as the end of the mushy zone and the value of f_1 at that point corresponds to the amount of the γ -Laves constituent that forms 'isothermally' at that location. Lastly, the f_1-x relation developed for the eutectic type transformations was joined to the f_1-x relation for primary solidification in order to construct the entire f_1-x curve in the mushy zone.

This method is obviously only an approximation as a number of simplifying assumptions are invoked, such as constant liquidus slopes and distribution coefficients, no significant effect from silicon during solute redistribution of the eutectic type reactions, and isothermal solidification of γ -Laves. Experimental measurement and use of liquidus slope values for niobium, silicon, and carbon are discussed below.

Liquidus slopes

The liquidus slopes for the 'solute' elements niobium, silicon, and carbon were determined by DTA. Liquidus temperatures for each alloy were determined by conducting slow heating rate (5 K min^{-1}) DTA scans. As an example, Fig. 8 shows a heating curve for alloy 3. On heating, a large endothermic peak associated with melting of the austenite matrix was initiated at 1366°C . Consistent with conventional DTA interpretations, the liquidus temperature is represented by the maximum on the peak occurring at 1413°C .^{8,9,14,15} Liquidus temperatures for all the alloys are given in Table 3. Average values and standard deviations



9 Comparison of measured liquidus temperatures with those calculated using equations (5a) and (5b)

for each liquidus temperature were determined from at least three measurements and the order of testing was random. The data show that the addition of each solute element lowered the liquidus temperature (see Table 1 for alloy compositions). The influence of each element can be determined by conducting multiple linear regression analysis on the DTA data.⁸ From this analysis, two linear equations were obtained

$$T_l = 1438 - 8.3(\%Nb) - 23.4(\%Si) - 34.1(\%C) \pm 2.8^\circ\text{C} \quad (5a)$$

for nickel base alloys and

$$T_l = 1448 - 10.3(\%Nb) - 7.6(\%Si) - 38.2(\%C) \pm 1.7^\circ\text{C} \quad (5b)$$

for iron base alloys, where contents are in wt-%. The liquidus slope of the *i*th solute in the system $m_{i,i}$ is given simply by

$$m_{i,i} = \partial T_l / \partial i \quad (6)$$

Table 3 Liquidus temperatures

Alloy	$T_l, ^\circ\text{C}$	Standard deviation,* K
1	1420.0	1.7
1.5	1418.0	0.3
2	1416.7	1.2
3	1412.3	0.6
3.5	1410.5	0.7
4	1407.3	0.6
5	1391.0	1.0
6	1390.0	1.0
7	1387.7	1.5
7.5	1382.0	1.4
8	1379.3	0.6
9	1430.4	0.9
10	1426.1	0.8
11	1423.9	1.1
11.5	1419.6	1.2
12	1418.8	0.2
13	1401.1	0.7
14	1392.0	0.3
15	1392.6	0.6
16	1385.6	0.3

* From at least three tests.

Thus, the coefficients in the multiple linear regression equations represent the liquidus slope of the particular element and the constants in the liquidus equations can be taken as T_0 in equation (3). These values are summarised in Table 4.

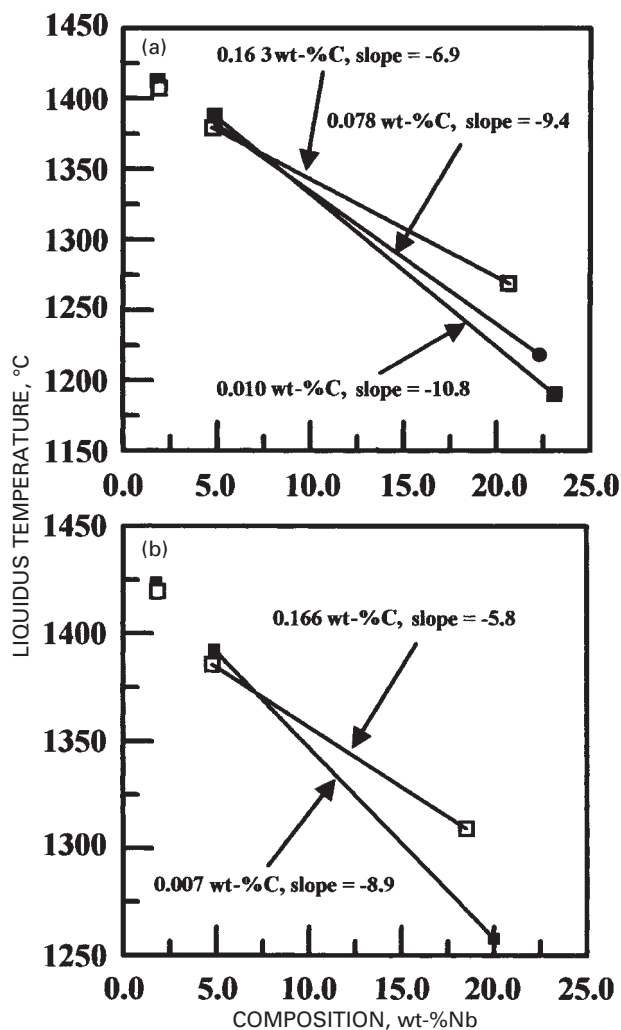
Figure 9 shows plots of measured liquidus temperatures *v.* those calculated using equations (5a) and (5b). The difference between measured and calculated temperatures never exceeded 2.8 K and was usually less than 1 K. Thus, simple linear regression equations provided an accurate representation of the solute effects. This result implies that interactive effects among the solutes over this rather limited composition range are negligible as no cross product terms were required in the linear regression equations. However, use of equation (3) required application of liquidus slope values over the entire solidification range from the liquidus temperature at the nominal alloy composition to the eutectic temperature where the primary solidification path strikes the line of twofold saturation. Thus, it is useful to consider how much the liquidus slopes may vary over the entire solidification range. While there were only enough experimental data to perform such an analysis for niobium, the result is useful for assessing possible variations in the liquidus slopes. This can be achieved by combining the liquidus data and nominal alloy compositions (from Tables 1 and 3) with the eutectic $L \rightarrow \gamma + NbC$ temperatures and compositions (from Fig. 7). At the eutectic composition, the eutectic temperature and liquidus temperature are synonymous. Thus, joining these two datasets essentially provided a view of the pseudoternary liquidus projection at constant carbon concentrations.

Figure 10 shows variation in liquidus temperature as a function of niobium content. The plot for the nickel base alloys (Fig. 10a) shows the variation in liquidus (and eutectic) temperature at low carbon content (alloys 3 and 7 contain 0.010 wt-%C), intermediate carbon content (alloys 3.5 and 7.5 contain on average 0.078 wt-%C), and high carbon content (alloys 4 and 8 contain on average 0.163 wt-%C). The eutectic compositions and temperatures were taken from Fig. 7a. Figure 10b shows similar data for the iron base alloys, but there were only enough data to plot slopes for low and high carbon contents. While the niobium liquidus slopes within the narrow composition range 2–5 wt-%Nb do not show significant dependence on carbon content and can therefore be represented by a single value (given in Table 4), the difference becomes significant when considered over a broader solidification range. The change in slope which occurs between the nominal niobium contents of 5 wt-% and the eutectic compositions are noted in Fig. 10. This difference occurs because, as shown in Fig. 7, the liquidus surfaces are curved and the region near the terminal $L \rightarrow \gamma + \text{Laves}$ reaction lies in a valley. As a result, the liquidus slopes increase (in absolute magnitude) as the carbon content decreases. Thus, use of constant liquidus slopes will lead to a discrepancy when the f_1-x calculations for the primary solidification mode are combined with those for the $L \rightarrow \gamma + NbC$ stage of solidification. This is apparent in Fig. 11, where the variation in temperature with f_1 in the mushy zone is shown for alloy 3.5.

The temperature regimes over which the primary $L \rightarrow \gamma$ and eutectic $L \rightarrow \gamma + NbC$ reactions occur are noted in Fig. 11. The dashed line shows the calculated results for the primary solidification stage using the constant liquidus slopes given in Table 4. When these values were used, the

Table 4 Liquidus slopes and T_0 values

Alloy	$m_{l,Nb}, \text{K/wt-\%}$	$m_{l,Si}, \text{K/wt-\%}$	$m_{l,C}, \text{K/wt-\%}$	$T_0, ^\circ\text{C}$
Ni base	-8.3	-23.4	-34.1	1438
Fe base	-10.3	-7.6	-38.2	1448



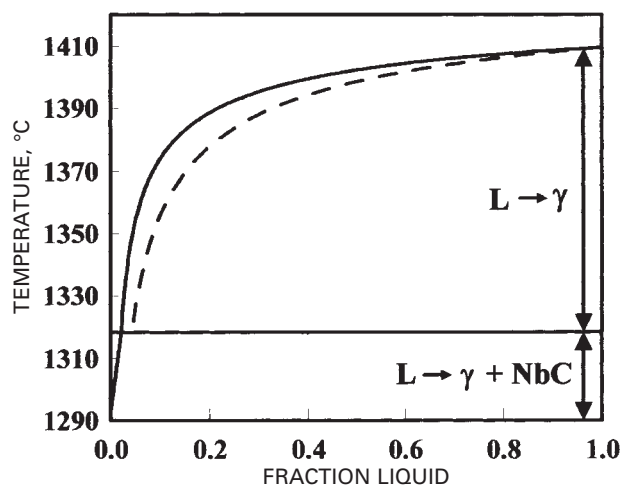
a for Ni base alloys; b for Fe base alloys

10 Variation in Nb liquidus slopes with nominal C content

temperature at any given f_l value was underpredicted and the curve for the primary solidification stage did not match properly to the curve for the $L \rightarrow \gamma + NbC$ eutectic portion of solidification. This occurred because the liquidus slopes decrease as solidification progresses, an effect which is not accounted for by use of a constant liquidus slope. The solid curve was recalculated by using effective slopes which were reduced by 34% from the values in Table 4 in order to force the plots from the primary and eutectic solidification stages to meet. Table 5 gives the amount each liquidus slope from Table 4 needed to be reduced by in order to maintain such consistency. For the nickel base alloys, the slopes of

Table 5 Change in liquidus slope values from Table 4 used in calculations

Alloy	Change, %	Alloy	Change, %
1	+14	8	-30
1.5	-16	9	+2
2	-16	10	-35
3	+4	11	-20
3.5	-34	11.5	-40
4	-2	12	-40
5	+22	13	-8
6	-20	14	-35
7	+6	15	-2
7.5	-28	16	-40



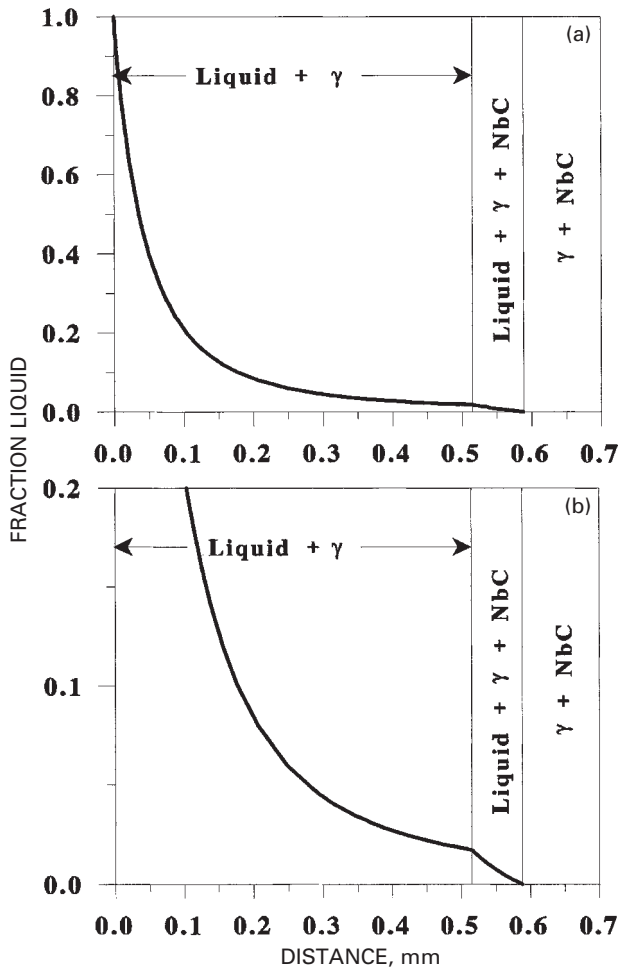
11 Variation in temperature with fraction liquid in mushy zone for alloy 3.5: dashed curve for primary solidification mode is calculated from liquidus slope values in Table 4, solid curve is calculated by reducing liquidus slope values in Table 4 by 34%

the low carbon alloys increased, while the slopes of the intermediate and high carbon alloys decreased. This is in agreement with Fig. 10a, in which the slope for the low carbon alloys is greater than the value of -8.3 K/wt-\%Nb given in Table 4, while the slopes became smaller than this value as the carbon content increased. For the iron base alloys, all the slopes needed to be decreased. The changes were generally small for the low carbon alloys while larger reductions were needed for the high carbon alloys. Again, this is consistent with Fig. 10b, in which the liquidus slope in the latter stage of solidification for the low carbon alloys is slightly lower than the value of -10.3 K/wt-\%Nb given in Table 4; the difference becomes larger as carbon content increases. While it is possible to account for such variations in the liquidus slopes during solidification by more complicated forms of equation (3), currently there are insufficient data to warrant such an approach and more complicated manipulations can obscure the main concepts. The results given in the present work are thus semiquantitative. Nevertheless, as discussed below, the calculated sizes of the mushy zones are realistic and the straightforward approach presented provides useful comparisons between alloys with variations in compositions without the need for more complicated mathematics.

Link between weldability and mushy zone characteristics

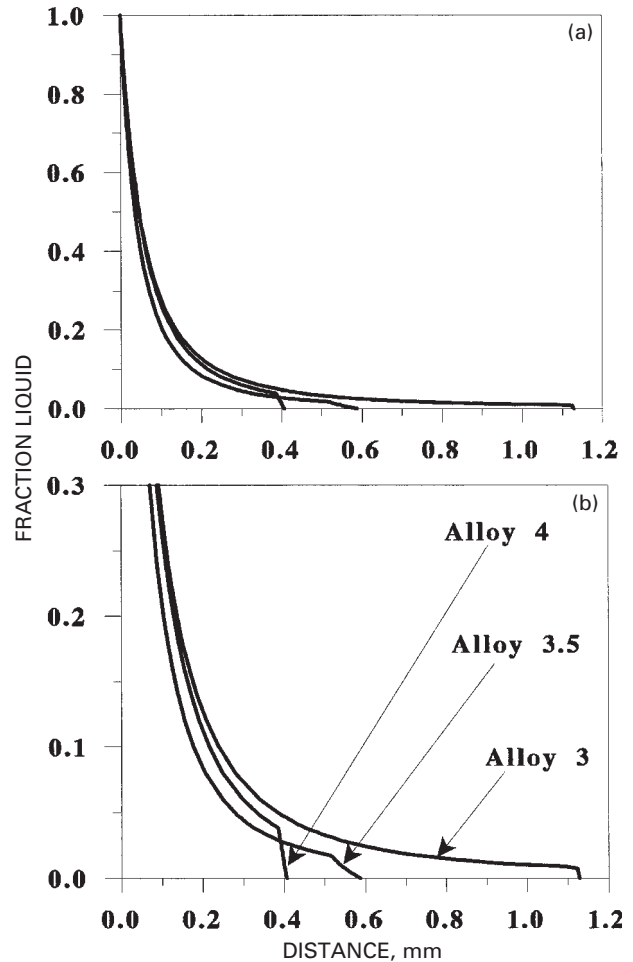
In the following section, calculations of mushy zone characteristics carried out using the procedure outlined above are described and combined with the weldability data presented in Fig. 6 to show how the results are useful for assessing composition-weldability relations. Figure 12 shows a typical f_l-x curve for alloy 3.5. Experimentally, this alloy terminated solidification with the $L \rightarrow \gamma + NbC$ reaction. Using Fig. 12, it is possible to determine the types of phases as a function of position in the mushy zone and such labels are provided on the curves.

Figure 13 compares the variation in f_l in the mushy zone for three alloys with essentially identical levels of niobium and silicon, but variations in carbon. Alloys 3.5 and 4 terminated solidification with the $L \rightarrow \gamma + NbC$ reaction, while the last remaining liquid in alloy 3 was enriched in niobium to the extent that solidification ended with the $L \rightarrow \gamma + \text{Laves}$ transformation. The kinks in the curves for alloys 3.5 and 4 mark the position where the $L \rightarrow \gamma + NbC$ reaction started. For alloy 3, primary solidification occurred



a over entire solidification range; b for $0 < f_1 < 0.2$

12 Calculated variation in fraction liquid with distance for alloy 3.5



a over entire solidification range; b for $0 < f_1 < 0.3$

13 Calculated variation in fraction liquid with distance for alloys 3, 3.5, and 4

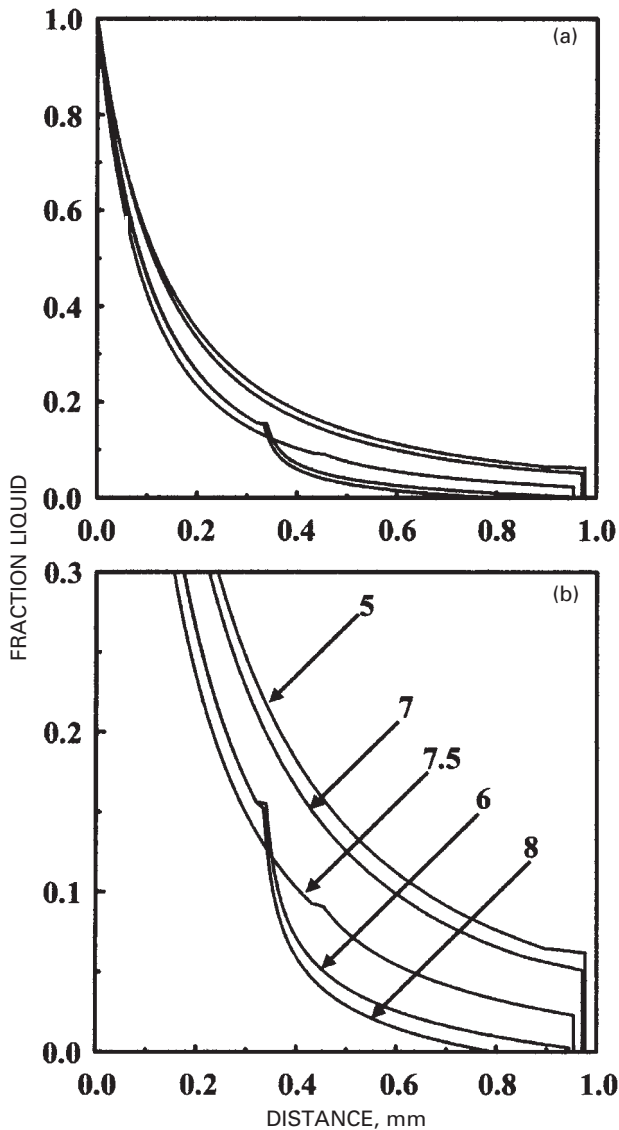
over a broad temperature range and very little eutectic type constituent was formed at the edge of the mushy zone. Since the primary solidification path for alloy 3 covers a broad temperature range, the mushy zone was relatively large. The effect of carbon content on the variation in f_1 with distance in the mushy zone is readily evident in Fig. 13. As the carbon content increased, the $L \rightarrow \gamma + \text{NbC}$ reaction occurred at higher temperatures and the reaction was therefore initiated at shorter distances behind the liquid weld pool. Once the reaction started, the remaining liquid was consumed over a short distance (small temperature range) and, in effect, 'closed up' the mushy zone. This is analogous to the behaviour expected in a simple binary system, except that the eutectic type transformation occurred over a temperature range rather than isothermally.

Figure 14 shows similar results for alloys 5–8. Experimentally, a small amount of liquid persisted after the $L \rightarrow \gamma + \text{NbC}$ reaction in these alloys and solidification terminated when this liquid transformed to the γ -Laves constituent. The effect of carbon is again readily apparent. When the $L \rightarrow \gamma + \text{NbC}$ reaction started in alloys 6 and 8, a relatively large amount of liquid was consumed over a short distance and the mushy zone tended to close up. In this particular case, the actual sizes of the mushy zones between the low and high carbon alloys were similar since the actual solidification temperature range for each alloy is similar. However, the high carbon alloys exhibited a smaller fraction of solute rich liquid near the trailing edge of the mushy zone. As explained in detail elsewhere, this small amount of terminal liquid leads to formation of the γ -Laves

constituent as isolated pockets where it is relatively harmless in terms of cracking susceptibility.¹⁶

Reference to the alloy compositions (Table 1) and the Varestreant data (Fig. 6) indicates that there is a critical amount of carbon needed for improved weldability in the iron base alloys. For example, alloys 11.5 and 12 have essentially identical levels of all other elements except carbon (alloy 12 contains 0.079 wt-%C and alloy 11.5 0.116 wt-%C). This small variation in carbon content led to a substantial difference in the MCL values. Within the iron base alloys with high niobium (alloys 13–16), carbon had no beneficial effect, even at the 0.21 wt-% level. Because of the high segregation potential of niobium in the iron base alloys, all of the iron base alloys will form the γ -Laves constituent. Thus, in order for carbon to provide improvements in cracking resistance, the C/Nb ratio must be high to cause the $L \rightarrow \gamma + \text{NbC}$ reaction to initiate at a relatively high temperature and a large amount of liquid should also be consumed during this step so that the amount of last residual liquid (which subsequently transforms to the γ -Laves constituent) is low enough to remain isolated near the edge of the mushy zone. In these alloys, the liquid remaining after the $L \rightarrow \gamma + \text{NbC}$ reaction should generally comprise below ~ 2.3 vol.-% to keep it isolated and thus deter any deleterious effect on cracking susceptibility.¹⁶

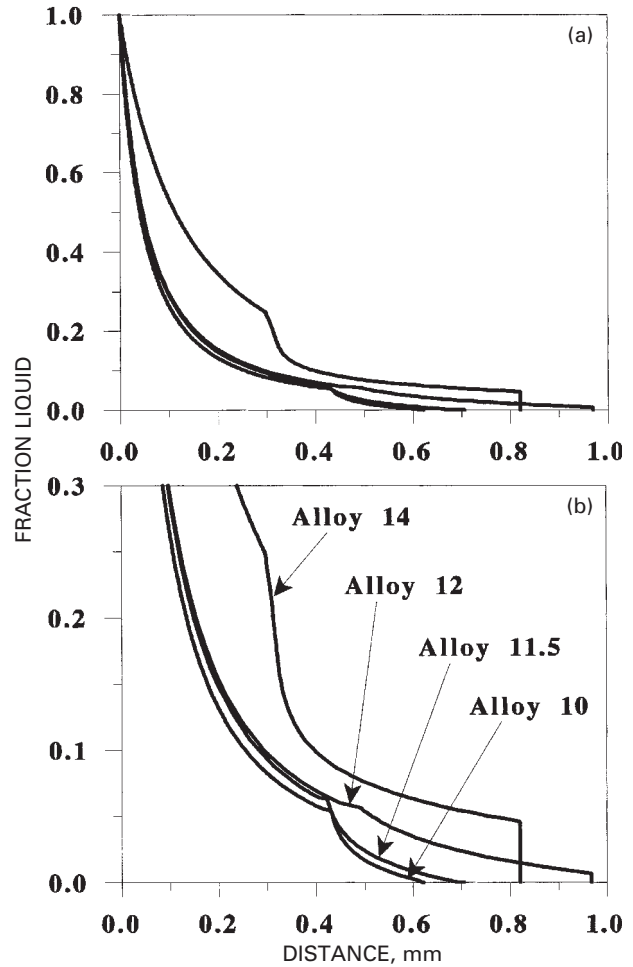
Figure 15 compares the f_1-x curves for iron base alloys, which showed a wide range in composition, mushy zone characteristics, and resultant solidification cracking resistance. Alloys 10 and 11.5 exhibit very similar curves in which the fraction liquid decreases very quickly near the



a over entire solidification range; b for $0 < f_l < 0.3$

14 Calculated variation in fraction liquid with distance for alloys 5, 6, 7, 7.5, and 8

edge of the mushy zone once the $L \rightarrow \gamma + NbC$ reaction is initiated. It should be noted that, experimentally, a very small amount of the γ -Laves constituent (< 1 vol.-%) did exist in these two alloys, implying that the last liquid became enriched to the point where the $L \rightarrow \gamma + Laves$ reaction is initiated. This indicates that the sizes of the mushy zones for these two alloys should be similar to that of alloy 12. Although the solute redistribution calculations are reasonably accurate, they are not sensitive enough to predict occurrence of the $L \rightarrow \gamma + Laves$ reaction in alloys 10 and 11.5. (Ref. 5). Nevertheless, the results are still useful for interpretation of the weldability data. Because a relatively large amount of liquid was consumed during the $L \rightarrow \gamma + NbC$ reaction for alloys 10 and 11.5, the last remaining liquid to undergo the $L \rightarrow \gamma + Laves$ reaction comprised less than 1 vol.-%. At this level, the γ -NbC always enveloped the γ -Laves and kept it isolated. An example of this for alloy 10 is shown in Fig. 16. This suggests that the last residual liquid was also isolated within the mushy zone during crack advancement. With this type of morphology, the isolated liquid pockets should have little deleterious effect and crack propagation through the entire mushy zone therefore is unlikely. The Varestraint data tend to support this. The MCL values for alloys 10

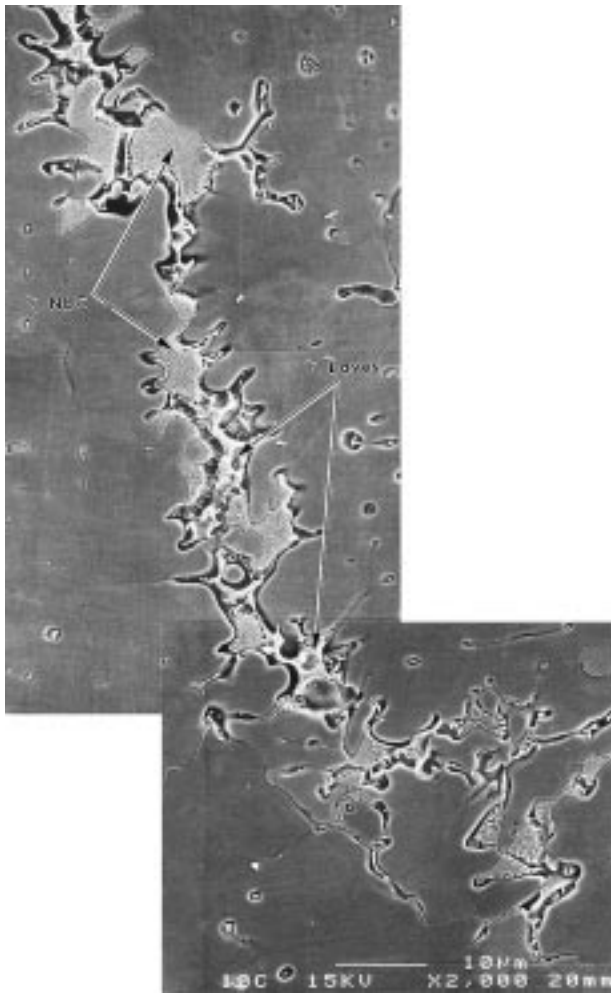


a over entire solidification range; b for $0 < f_l < 0.3$

15 Calculated variation in fraction liquid with distance for alloys 10, 11.5, 12, and 14

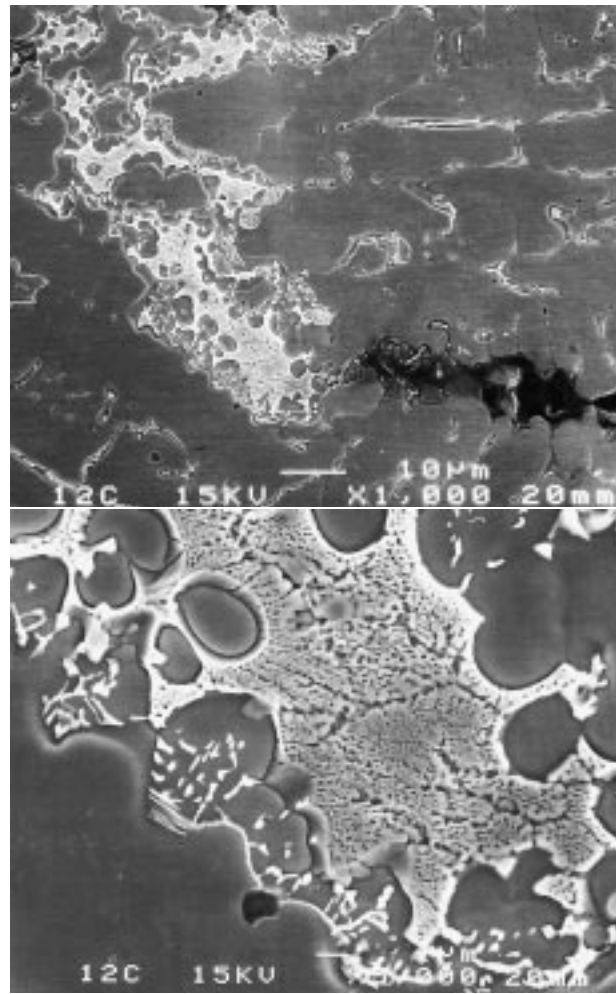
and 11.5 are only 0.67 and 0.89 mm respectively, only slightly higher than the range of 0.41–0.64 mm observed in the alloys that form no γ -Laves and have excellent weldability. In contrast, Fig. 15 shows there was always more residual liquid available for the low temperature $L \rightarrow \gamma + Laves$ transformation in alloy 12. As a result, this residual liquid existed as a continuous network and crack propagation through the entire mushy zone was more favourable. This is reflected in the Varestraint data, as the MCL in alloy 12 of 1.65 mm is considerably greater than those in alloys 10 and 11.5. An example of the continuous γ -Laves morphology in alloy 12 is shown in Fig. 17. In addition, this MCL value is similar to that of alloy 14 (1.53 mm), which also exhibited γ -Laves in a continuous network (Fig. 18). The slightly shorter crack length of alloy 14 can be attributed to its lower liquidus temperature: the value of T_l for alloy 12 is 1419°C while that for alloy 14 is 1392°C.⁴ This difference is caused by the higher contents of niobium and carbon in alloy 14. A decrease in the liquidus temperature causes an effect similar to an increase in the terminal solidus temperature; it reduces the solidification temperature range and resultant size of the crack susceptible mushy zone.

The results above indicate that cracking susceptibility depends not only on the solidification temperature range, which controls the total length of the mushy zone, but that cracking behaviour is also sensitive to the amount and distribution of liquid at the trailing edge of the mushy zone. Liquidus temperatures (Table 3) and eutectic temperatures can be used to determine the solidification temperature



16 Scanning electron micrographs showing morphology of γ -NbC and γ -Laves constituents in solidification cracks of alloy 10

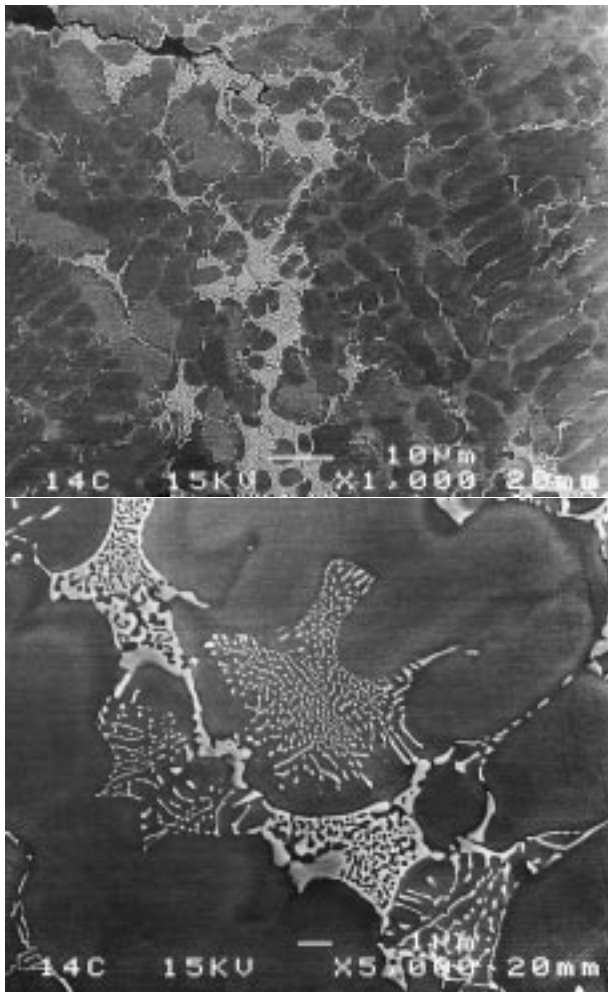
range of each alloy. The solidification temperature range is most appropriately given by the difference between the liquidus temperature determined from DTA heating scans and the terminal eutectic temperature measured during cooling.^{20,21} The on heating liquidus temperature was used since the weld metal solidifies epitaxially from the base metal and requires no undercooling.²¹ Temperatures of eutectic type reactions and the solidification temperature range ΔT of each alloy are given in Table 6. All alloys, except alloys 2, 3.5, and 4, exhibited the γ -Laves eutectic type constituent. Thus, the temperature of the $L \rightarrow \gamma + \text{Laves}$ reaction should be used as the value for the terminal solidus temperature for all alloys except 2, 3.5, and 4. For the nickel base alloys, the γ -Laves constituent formed in very small amounts, which precluded measurement of the $L \rightarrow \gamma + \text{Laves}$ reaction temperature by DTA. The temperature for this reaction was estimated to be 1190°C with a 17.8 wt-%Nb alloy which formed a large amount of the γ -Laves constituent and produced a large exothermic DTA peak associated with the $L \rightarrow \gamma + \text{Laves}$ reaction. Measurements by EPMA showed that the composition of the γ -Laves constituent in the high niobium alloy was very similar to that observed in the nickel base alloys.⁴ Thus, the reaction temperature measured for this high niobium alloy should serve as a good estimate for the terminal solidus temperatures of the nickel base alloys which complete solidification by the $L \rightarrow \gamma + \text{Laves}$ reaction. The $L \rightarrow \gamma + \text{Laves}$ reaction temperature could not be measured directly in the iron base alloys with low niobium. The



17 Scanning electron micrographs showing morphology of γ -NbC and γ -Laves in solidification cracks of alloy 12

values measured in the high niobium, iron base alloys exhibit a fairly narrow range of 13 K. Thus, the average of these values should provide a good estimate for the low niobium alloys. For alloys 2, 3.5, and 4, the terminal solidus is taken as the value measured for the $L \rightarrow \gamma + \text{NbC}$ reaction as no γ -Laves constituent was observed. Positive identification of secondary phases could not be made in alloys 1 or 1.5, so no solidification temperature range is reported for these alloys.

Figure 19a shows a plot of MCL as a function of the solidification temperature range and no correlation is readily apparent. Five of the alloys (6, 7.5, 8, 10, and 11.5) exhibited a rather wide solidification temperature range, but show good weldability (low MCL). This lack of correlation between the MCL and ΔT has also been observed by Cieslak²⁰ in systematic composition variations in the niobium bearing superalloy IN 625. The alloys with high ΔT but low MCL initiated the $L \rightarrow \gamma + \text{NbC}$ reaction at a short distance behind the edge of the weld pool and much of the remaining liquid was consumed over a relatively short distance, which tends to close the mushy zone. As a result, the amount of terminal liquid which underwent the $L \rightarrow \gamma + \text{Laves}$ reaction was always less than ~ 2 vol.-% and remained isolated (see Fig. 16 for an example). This type of morphology should resist crack propagation throughout the mushy zone, so the effective terminal solidus temperature for these alloys should more accurately be represented by the temperature of the $L \rightarrow \gamma + \text{NbC}$ reaction. The MCL and ΔT data are replotted in Fig. 19b using this terminal solidus temperature and the trend between cracking



18 Scanning electron micrographs showing morphology of γ -NbC and γ -Laves in solidification cracks of alloy 14

susceptibility and the effective solidification temperature range is apparent. This improved correlation indicates that cracking susceptibility depended on both the solidification

temperature range and the amount and distribution of terminal liquid at the edge of the mushy zone. The solidification temperature range essentially controlled the total distance over which crack propagation was possible, while the amount and distribution of terminal liquid affected how far the crack travelled through the edge of the mushy zone.

The calculated f_1-x curve for alloy 7.5 represents the only exception among the five alloys discussed above. The calculated decrease in f_1 at the edge of the mushy zone occurred rather gradually and was similar to that for alloy 12, which displayed relatively poor weldability. Quantitative image analysis indicated that each of these two alloys formed $\sim 2.3 \pm 0.8$ vol.-% of the γ -Laves constituent (the terminal liquid) and similar levels of the γ -NbC constituent (5.2 ± 0.5 vol.-% in alloy 7.5 and 4.4 ± 1.7 vol.-% in alloy 12). However, examination of the solidification cracks in alloy 7.5 (Fig. 20) showed that, unlike alloy 12 (Fig. 17), the γ -Laves constituent was always isolated. Thus, these two alloys are very close to the critical amount of terminal liquid which can be tolerated before that terminal liquid becomes continuous. The small difference which produced the significant change in cracking behaviour could not be discerned in the QIA results because γ -Laves formed in such small amounts and the assumptions made in the calculations preclude the distinction of such fine detail in the f_1-x curves. This suggests that the calculated results can be difficult to interpret for weldability predictions among alloys with such similar behaviour. However, the f_1-x diagrams described in the present work are generally useful for understanding how nominal alloy composition influences the variation in f_1 with distance in the mushy zone which, in turn, is helpful for understanding the potential cracking behaviour through the mushy zone. The approach developed above is general in nature and therefore is applicable to other alloy systems when the appropriate phase diagram quantities are known from experimental data, or can be estimated from thermodynamic databases, and interactive effects among solutes are not large.³

CONCLUSIONS

The solidification and weldability of multicomponent nickel base and iron base superalloys with systematic variations in composition have been investigated through Varestment testing and solute redistribution modelling. Solute redistri-

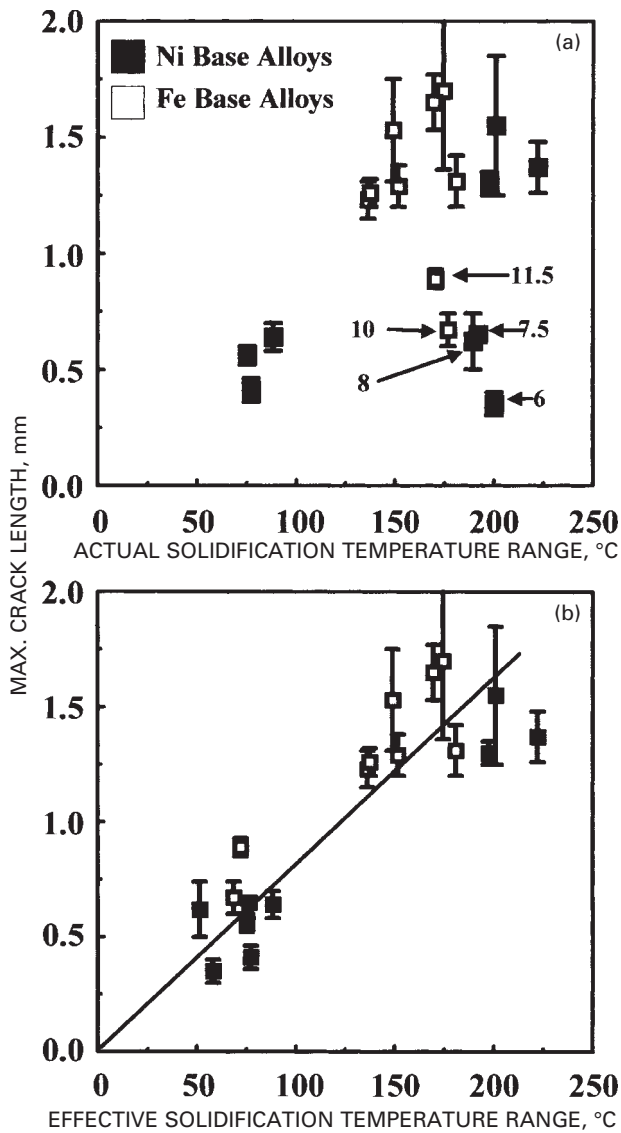
Table 6 Reaction temperatures and solidification temperature ranges ΔT

Alloy	L \rightarrow γ + NbC		L \rightarrow γ + Laves		ΔT , K
	Reaction temperature, °C	Standard deviation,* K	Reaction temperature, °C	Standard deviation,* K	
2	1341.5	0.7	†	†	75.2
3	‡	‡	1190.0	...	222.3
3.5	1322.0	1.4	†	†	88.5
4	1330.0	1.3	†	†	77.3
5	‡	‡	1190.0	...	201.0
6	1332.0	1.4	1190.0	...	200.0
7	‡	‡	1190.0	...	197.7
7.5	1305.5	0.7	1190.0	...	192.0
8	1328.0	2.8	1190.0	...	189.3
9	‡	‡	1249.3	...	181.1
10	1357.5	0.7	1249.3	...	176.8
11	‡	‡	1249.3	...	174.6
11.5	1347.5	2.1	1249.3	...	170.3
12	1348.0	1.4	1249.3	...	169.5
13	1332.5	0.7	1249.5	3.5	151.6
14	1360.8	2.2	1243.0	2.1	149.0
15	1289.5	0.8	1256.3	1.2	136.3
16	1355.2	1.7	1248.2	4.8	137.4

* From at least three tests.

† Not applicable.

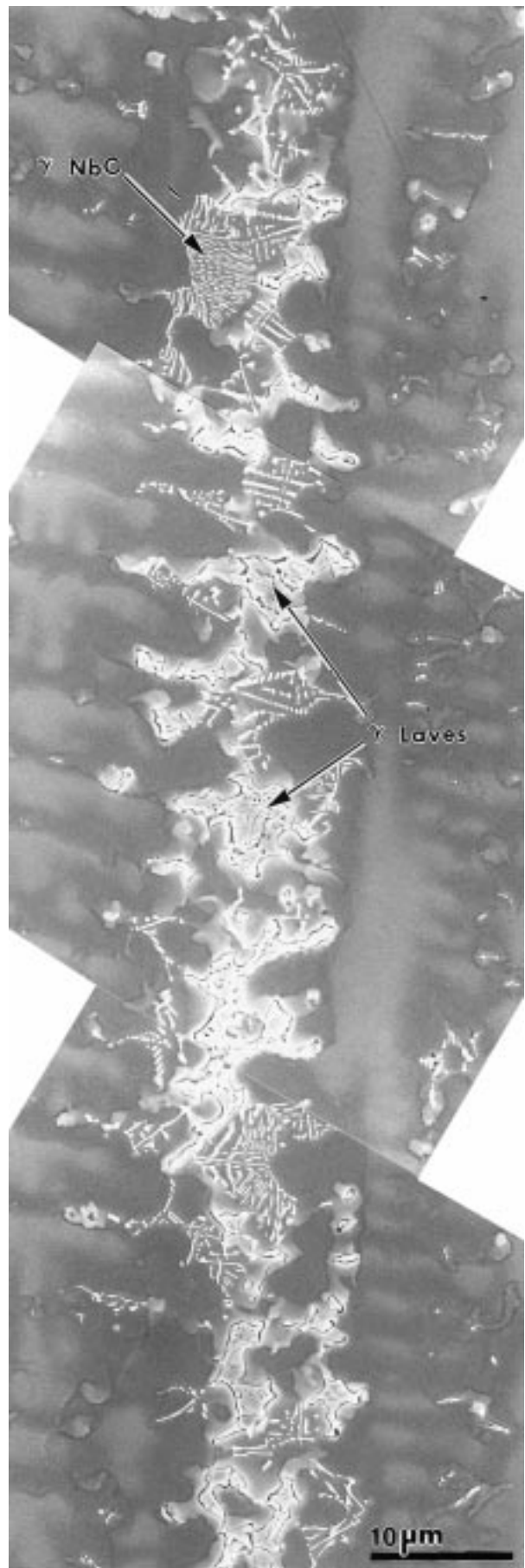
‡ Not determined.



a as function of actual solidification temperature range; b as function of effective solidification temperature range

19 Maximum crack length

tribution models were linked to the general liquidus equation of a multicomponent system and temperature gradient information to calculate how the variation in fraction liquid within the crack susceptible mushy zone is affected by alloy additions. Solidification parameters of each solute, such as the liquidus slope and distribution coefficient, were experimentally determined and used as inputs to the model calculations. Carbon additions to all the nickel base alloys consistently provided significant improvements in solidification cracking resistance. The modelling results directly show that carbon additions to these alloys reduce the size of the crack susceptible mushy zone by increasing the start temperature of the $L \rightarrow \gamma + \text{NbC}$ reaction and limiting the amount of liquid which exists for the low temperature $L \rightarrow \gamma + \text{Laves}$ transformation. Carbon additions to the iron base alloys were only beneficial when the niobium content was low (~ 1.8 wt-%) and the carbon content had to be above ~ 0.1 wt-%. In this case the modelling results show that, primarily as a result of the increased segregation potential of niobium, the iron base alloys will exhibit more solute rich liquid near the edge of the mushy zone which undergoes the low temperature $L \rightarrow \gamma + \text{Laves}$ transformation. This effectively makes the mushy zone more susceptible to solidification cracking. The calculation procedure described



20 Scanning electron micrographs showing morphology of $\gamma\text{-NbC}$ and $\gamma\text{-Laves}$ constituents in solidification cracks of alloy 7.5

in the work is general in nature and is applicable therefore to any binary or multicomponent alloy system when the proper phase diagram quantities and solute redistribution behaviour are known.

ACKNOWLEDGEMENTS

The authors would like to thank Dr M. J. Cielsak at Sandia National Laboratories (SNL) for useful discussions and review of the manuscript. They would also like to thank the anonymous reviewer who provided many useful comments on the manuscript. One author (JND) gratefully acknowledges financial support for this research from the American Welding Society Fellowship Award. Preparation of the experimental alloys by B. Damkroger and M. Maguire at SNL is also greatly appreciated. Sandia Corp., a Lockheed Martin Co., operates SNL as a multiprogram establishment for the United States Department of Energy under contract no. DE-AC04-94AL85000.

REFERENCES

1. T. W. CLYNE and G. J. DAVIES: Proc. Conf. 'Solidification and casting of metals', Sheffield, UK, July 1977, 275-278; 1979, London, The Metals Society.
2. J. A. BROOKS: Proc. Conf. 'Weldability of materials', 41-48; 1990, Materials Park, OH, ASM International.
3. B. SUNDMAN, B. JANSSON, and J. O. ANDERSON: *Calphad*, 1985, 9, 153-190.
4. J. N. DUPONT, C. V. ROBINO, A. R. MARDER, M. R. NOTIS, and J. R. MICHAEL: *Metall. Mater. Trans. A*, 1998, **29A**, 2785-2796.
5. J. N. DUPONT, C. V. ROBINO, and A. R. MARDER: *Acta Mater.*, 1998, **46**, (13), 4781-4790.
6. W. F. SAVAGE and C. D. LUNDIN: *Weld. J. Res. (Suppl.)*, 1965, **44**, 433s-442s.
7. W. F. SAVAGE and C. D. LUNDIN: *Weld. J. Res. (Suppl.)*, 1966, **45**, 497s-503s.
8. M. J. CIESLAK, T. J. HEADLEY, T. KOLLIE, and A. D. ROMIG, JR: *Metall. Trans. A*, 1988, **19A**, 2319-2331.
9. Y. NAKAO, H. OHSHIGE, S. KOGA, H. NISHIHARA, and J. SUGITANI: *J. Jpn Weld. Soc.*, 1982, **51**, 989-995.
10. H. H. STADELMAIER and M. L. FIEDLER: *Z. Metallkd*, 1975, **66**, (4), 224-225.
11. B. RADHAKRISHNAN and R. G. THOMPSON: *Metall. Trans. A*, 1989, **20A**, 2866-2868.
12. R. MEHRABIAN and M. C. FLEMINGS: *Metall. Trans. A*, 1970, **1**, 455-464.
13. T. W. CLYNE and W. KURZ: *Metall. Trans. A*, 1981, **12A**, 965-971.
14. G. A. KNOROVSKY, M. J. CIESLAK, T. J. HEADLEY, A. D. ROMIG, JR, and W. F. HAMMETTER: *Metall. Trans. A*, 1989, **20A**, 2149-2158.
15. M. J. CIESLAK, T. J. HEADLEY, G. A. KNOROVSKY, A. D. ROMIG, JR, and T. KOLLIE: *Metall. Trans. A*, 1990, **21A**, 479-488.
16. J. N. DUPONT, C. V. ROBINO, and A. R. MARDER: *Weld. J. Res. (Suppl.)*, 1998, **77**, 417s-431s.
17. J. C. BORELAND: *Br. Weld. J.*, 1960, **7**, 508-512.
18. E. SCHEIL: *Z. Metallkd*, 1942, **34**, 70.
19. J. N. DUPONT: PhD thesis, Lehigh University, Bethlehem, PA, USA, 1997.
20. M. J. CIESLAK: *Weld. J. Res. (Suppl.)*, 1991, **70**, 49s-56s.
21. S. A. DAVID and J. M. VITEK: *Int. Mater. Rev.*, 1989, **34**, (5), 213-245.

Marangoni and Interfacial Phenomena in Materials Processing

Originating from Contributions to a Discussion of the Royal Society of London

Organized and Edited by

E.D. Hondros, M. McLean and K.C. Mills

B692 ISBN 1 86125 056 8 Hardback 268pp

European Union £45/Members £36

Non-European Union \$90/Members \$72

p&p European Union £5.00/Non-EU \$10.00 per order

Orders to: IOM Communications Ltd, Shelton House, Stoke Road, Shelton,
Stoke-on-Trent ST4 2DR Tel: +44 (0) 1782 202 116 Fax: +44 (0) 1782 202 421

Email: Orders@materials.org.uk Internet: www.materials.org.uk

VAT Registration No. GB 649 1646 11 Reg. Charity No. 1059475



IOM Communications

IOM Communications Ltd is a wholly owned subsidiary of the Institute of Materials